AN ELECTROSTATICALLY SUSPENDED, MICRO-MECHANICAL RATE GYROSCOPE

NASA Contract # NAS1-19282

Timothy Hawkey
Richard Torti
SatCon Technology Corporation
12 Emily Street
Cambridge, MA 02139

1. Introduction

SatCon Technology has performed a study of micromechanical gyroscopes. The goals of this Phase I SBIR program were to define a baseline system configuration and establish technical feasibility for Phase II proof of principle, prototype fabrication. This report documents the research and presents the baseline mechanical design, sensors, control system, and electronics. This section presents a project overview and specific technical objectives. Section 2 contains a background on micromechanical technology, Section 3 the microgyroscope specifications and configuration, and Section 4 the electromechanical design. Section 5 outlines the control and electronics. Section 6 presents a preliminary sequence for microfabrication of the baseline design, and Section 7 conclusions and recommendations for further work.

2. Background

Micro-electronic fabrication technologies have recently been applied to produce novel micro-mechanical devices such as motors, pressure sensors, and linear actuators. Their small size, possible integration with electronic circuits, and potential low cost invite research. Thus far, however, few useful devices have been developed. A micro-mechanical gyroscope, proposed for this research effort, is a device that would have application to aerospace, commercial, and military systems. They could eventually be available for low cost and see widespread use in integrated navigation and control systems for micro-satellites, airplanes, and terrestrial or planetary autonomous vehicles. Other potential applications include automobiles and in control units for robotic end effectors.

The last twenty years have seen a revolution in the micro-electronics industry. Since the development of the first integrated circuit of a few transistors in the early 1970s, micro-processors over a million transistors are now routinely fabricated. In the last several years, techniques have been borrowed from the chip industry and used to fabricate micro-mechanical devices. Generally, these techniques fall into two categories, bulk micromachining and surface micromachining. A good overview of micromechanical fabrication can be found in Reference 1[1].

2.1 Bulk Micromachining

Bulk micromachining involves direct modification of silicon wafers with chemical etchants. Silicon crystal, it was discovered in the 1950s, can have its different crystal planes selectively etched by alkaline solutions at precise angles. Portions of the wafer can be protected by layers of silicon dioxide or silicon nitride (standard microelectronic materials) or ion implantations of boron. Bulk micro-machining is commonly used to fabricate trenches, cantilevers, cavities, nozzles, and membranes. An important associated technology to bulk micromachining is wafer bonding. Wafer bonding processes, first developed in the 1960s allow the fusion of silicon wafers together at the atomic level without adhesives. Infrared alignment devices allow wafer alignments accurate to about 1 micron.

2.2 Surface Micro-machining

Surface micromachining differs from bulk micro-machining in that most of the work is done on top of the wafer. Structural and sacrificial films are deposited on top of the wafer. After deposition, the sacrificial layers are selectively etched, leaving the micromechanical structure behind. Westinghouse Research Laboratories first applied the technique with metal films in the 1960s. In the early 1980s, researchers began using silicon dioxide as a sacrificial layer, and polycrystalline silicon as a structural material. Chemical vapor deposition (CVD) and

photolithography are used to grow the layers on the wafer and chemical or reactive ion etching (RIE) is used to remove sacrificial layers. Complex structures such as motors and linear actuators have been developed, but the lithographic processes limit the thickness and number of layers that can be patterned in this way. Each layer can be at most 3 or 4 μ thick, and structures of more than 5 layers are difficult to fabricate. Currently, standard micro-electronic materials, silicon dioxide, silicon nitride, and poly silicon are almost exclusively used in surface micromachining. Other materials such as aluminum and polyimide are being investigated and hold promise for opening new possibilities in surface micromachining.

2.3 Other Microfabrication Techniques

Surface and bulk micromachining can be used to produce a fascinating array of microdevices, but they are limited to thin film configurations for surface machined structures and the crystal planes of silicon for bulk micromachined devices. Other techniques currently under development may allow a wider range of configurations and devices to be fabricated in the future. One possibility is deep X-Ray or short ultraviolet lithography. The shorter wavelengths of X-Ray and UV radiation allow taller patterns to be produced without sacrifice in edge clarity. Other possibilities include micro electric-discharge machining (EDM) and a German developed process called LIGA which uses X-Ray fabricated, plated molds that are used to form microstructures that may be more than 100 μ tall with lateral features in the 3 μ range.

2.4 Micro-dynamics

A fundamental issue in micromechanics is the scaling of physical forces and properties in the micron domain. Some forces scale directly with object size, others with the square or cube. Mass, and hence weight scale with the object volume and decrease cubically with size. Magnetic field forces scale with area as do electric field forces. Force and torque production for electromechanical actuators are controlled by air gap energy storage. The limits on energy storage are set by metal saturation flux density in magnetic devices for magnetic field devices and electric field breakdown strength for electric devices. Typical saturation fields of 2 tesla and typical electric field breakdown of 3×10^6 volts/meter show energy storage densities of 1.6×10^6 J/m^3 and 40 J/m^3 respectively, explaining the preponderance of magnetic motors. For very small air gaps, however, the electric field breakdown strength increases substantially. At micron level, the electric field breakdown strength is greater than 10^8 volts/meter, allowing similar energy storage densities in electric and magnetic fields. Given the difficulties of microfabricating magnets and three dimensional coils, electric field actuation is generally preferable in microdevices.

3. Specifications and Configuration.

As with all sensors, resolution, accuracy, large dynamic range, low power consumption, small size and high bandwidth are desired. For this technology effort, the obvious primary objective was small size with the goal of eventually developing a complete two-axis rate gyro on a microchip. Maximum/minimum angular rates of 10 radians/sec and 0.1 radians/sec and 200 Hz bandwidth were chosen as specification goals to approximate what might be required for use on robotic arms. Other performance specifications were determined by process controlled geometries and parameters as discussed in Section 4.

3.1 Suspended Gyro Configuration

The initial micro-gyro configuration identified is shown in Figure 1. Configured as a

rebalance gyro, this microfabricated machine consists of three types of electroquasistatic components - the motor drive, position sensors, and the non-rotary actuators for rebalance and suspension. Like suspended macroscopic gyros, the rotor is spun by a motor to produce angular momentum, suspended and controlled by force and torque actuators, and sensed by various position sensors. As discussed in Section 2, all the sub-components are electric field devices. The term "rebalance" identifies the gyro mode of operation. When acted on by external forces, the control system is designed to hold the gyro in a constant position, rebalancing it. Knowledge of the actuator control signals and dynamics allows the inputs to be determined. Since the controlled mass (the gyro rotor in this case) is held to a nearly constant position, the linearity of the sensors and actuators is improved, and the overall dynamics are simplified. The block diagram is shown in Figure 2.

The electrostatic force can be written in linearized form for a fixed potential as

$$F=\frac{1}{2}V^2\frac{\partial^2 C}{\partial^2 X}\Delta X$$

where ΔX represents the excursion about the equilibrium position, and the coefficient is positive. Since the force increases with decreasing distance, the motion is unstable and without other compensation requires closed loop control. In the case of a fully suspended rotor, this control must be effected in both axial and radial directions (five unstable degrees of freedom). There are therefore four sets of actuator/sensors - two for the upper and lower axial suspension and two for upper and lower radial rebalance actuator/sensors - and the motor driver actuator. Hence the multilayered configuration of the figure.

The fabrication of such a multi-actuated, multi-sensed device requires at least five sets of alternating insulating/conducting layers on the rotor. For reasonable capacitive bias currents and actuator forces, the facing areas must be at least 1-2 μm high with radial gaps of the same order. The height of this rotor will accumulate to over 5μm. Present technology, however, only makes feasible aspect ratios (rotor thickness to gap) of up to 2/1, with 1/1 being typical. This gap in fabrication technology will have to be bridged to allow successful fabrication of a fully suspended micro-gyro.

3.2 Top Configuration

An alternate arrangement which has the advantage of using largely successful fabrication techniques is the supported top shown in Figure 3. In this case only two layered sets are used, the radial gap motor drive and the bottom actuator/sensor. The "top" has only two unstable degrees of freedom--the two tilt angles about the pivot point. The axially facing sensor/actuator provides an enhancement in capacitance over the radial gap approximating the ratio of rotor radius to height. Both sensing and actuation are accomplished with four electrodes imbedded the plane of the substrate as shown in Figure 3. If ohmic continuity is assured from the rotor bottom plate through the support spindle and into the substrate, the values of the four variable capacitors can be used to sense the direction of the inclination of the rotor axis for the normal to the substrate plane. Since this configuration will likely be first constructed as a preliminary to a fully suspended prototype, the remainder of the Phase I work focused on this configuration.

3.3 Motor Configuration

The electrostatic production of torque has long been considered for motor drives. Four classes of electroquasistatic motor actuators have emerged which have analogues with magnetically operated devices - variable capacitance, electrostatic induction, permanent electret, and electric hysteresis. In the work by Bart[2] induction and variable capacitance motors were studied in detail with attempts made to fabricate both axial gap and radial gap variable capacitance motors. Axial gap motors have not yet successfully been fabricated, but radial gap variable capacitance motors have been built and tested at both MIT and Berkeley. Our system therefore baselined a radial gap motor as fabricated at MIT (see Bart).

3.2 Sensor Configuration

The baseline sensor configuration chosen was capacitive position sensing using a superposition of high frequency signals between the axial control electrodes and the rotor. Decomposition of the four sensor signals (one for each axial stator electrode) provides the signals needed to control the rotor. Capacitive position sensing is commonly used in macroscopic devices, and has also been successfully applied to other micromechanical devices. The basic concept is to drive a constant current across an air gap (whose capacitance varies inversely with gap distance) and read the resulting voltage which is linearly proportional to the gap. High frequency modulation and demodulation allow good noise immunity. Though the capacitance of the microgyro axial gap will be very small (about 3×10^{-14} farads), the placement of FETs (field effect transistors) on the silicon substrate as preamplifiers as done by Schmidt[3] should allow reasonable measurements to be made.

4. Electromechanical Design

The design of the motor drive and rebalance actuator is based upon the specifications discussed in Section 3 many of which were derived from known fabrication constraints and experience. Dimensions were generally conservatively chosen given the uncertainty in fabricating devices with this technology.

4.1 Sizing

The overall rotor diameter, 200 μ, was chosen as the largest size that could be fabricated without significant warpage due to residual stress buildup during fabrication. The rotation rate is constrained by stress limits in the rotor and electronics limits in the motor driver circuitry. A rate of 500,000 rpm (8.3 kHz) was chosen as a reasonable extension of current motor rates (about 20,000 rpm). This is well below the ultimate spin rate (about 10,000,000 rpm) determined by material strength limits. The required electronics frequency, 25 kHz, is attainable without excessive noise problems. The motor height was set to 2.2 μ, the same height as currently fabricated micromotors. The maximum value of total rotor thickness is limited by fabrication technology to about 2 times the radial gap of 1.5 μ. The axial gap between substrate and rotor was set at 2 μ. This represents a tradeoff between gap capacitance and rotor unstable frequency. A smaller gap would make sensor measurements more accurate at the cost of raising the unstable frequency and complicating the control problem. The 2 μ gap gives a 300 Hz unstable frequency.

4.3 Sensor

The four segment rebalance sensor/actuator electrode design is similarly derived from the specifications. While it was not attempted to optimize the pattern for torque, depositing the

conducting region from 0.7 R to 1 R gives adequate rebalance torques and adequate capacitance for sensing inclinations as small as 0.008°. A possible difficulty is the actually attainable depth and uniformity of the implanted electrodes since the thermal noise limit is sensitive to circuit resistance. The sensor capacitance between each of the four electrodes and the rotor is approximately $3x10^{-14}$ F. With a typical commercial oscillator frequency of 100 kHz, the sensor current is about 15 nA for operation at 0.8v. Since commercial devices sense capacitance in the same range (although with larger electrode and gaps) it should be possible to use standard techniques for angle information.

4.4 Summary

The tables below give a summary of the dimensions and parameters predicted for the two degree of freedom microgyro.

Spin Angular Speed	500 kRPM
Spin Moment of Inertia	1.5x10-18 kgm-m2
Precession Moment of Inertia	8x10-19 kgm-m2
Minimum Angular Rate	0.01°/s
Thermal Sensor Noise	< 0.4x10-3 v
Angular Sensitivity	< 0.008°
Sensor Electrode Capacitance	3x10-14 F
Sensor Operating Current (0.8 V)	15 x10-9 A
Nominal Drive Actuator Potential	0.5 v
Drive Torque Per Pole	10-11 N-m
Rotor Radius	50μm
Radial Gap	1.5 μm
Vertical Gap	2 μm
Rotor Thickness	2.2 μm
# Stator Poles	12
# Rotor Poles	8

5. Control and Electronics Design

This section presents the controller design and closed-loop simulations of expected dynamic performance. As shown in Figure 2, and described previously, the system block diagram consists of the actuator and plant (gyroscopic) dynamics, the sensors, the controller, and the decomposition electronics. One of the goals of the controller is to keep the orientation of the rotor fixed, in the null position, relative to the orientation of the "stator" frame of the gyroscope. In addition, the controller must provide accurate measurement of the torque that is required to maintain the rotor in the null relative orientation. As usual, the simplest controller that can meet the performance objectives is desired, in order to minimize hardware complexity. In particular, a fixed-gain, linear controller is desired that can be easily implemented in analog electronics. This will force some performance and stability robustness tradeoffs, in particular because the plant dynamics are a strong function of the operating speed and are open-loop unstable. Because of the open-loop unstable nature of the plant -- an inverted pendulum at low speeds -- closed-loop control is required from zero speed to the full operational speed. The challenge, then, is to find a fixed gain controller that will provide adequate performance at all speeds.

5.1 Open-Loop Plant Dynamics

The variation of the plant dynamics from zero speed to operational speed of 500,000 rpm (8,333 Khz) is dramatic. At zero speed, the plant is a two-degree-of-freedom unstable pendulum. The two by two plant transfer function matrix relating control voltage inputs to rotor orientation output becomes diagonal in this case, with no cross-coupling between the x-direction tilt dynamics and the y-direction tilt dynamics. At zero speed, therefore, the plant can be treated as two identical single-input, single-output (SISO) systems. The important dynamics of the zero-speed plant can be seen in the Bode plots of the plant transfer functions (control voltages to rotor orientations) shown in Figure 4 below. Since the off-diagonal or cross-coupling transfer functions (x voltage to y orientation, y voltage to x orientation) are zero at zero speed, and the diagonal transfer functions are identical, only one transfer function is seen in Figure 4. At frequencies below 300 Hz, the dynamics of this parallel or diagonal transfer function are seen to be dominated by the unstable torsional spring produced by the combination actuator and motor torsional effects. The unstable spring produces the flat low frequency magnitude response between input voltage (torque) and output orientation (angle) with the 180 degrees of phase indicating an unstable spring. At frequencies above the 300 Hz unstable frequency, the transfer function falls off with a slope of minus two, caused by the double integration of torque to angle, and scaled by the voltage to torque constant (ba) and the radial moment of inertia of the rotor (Irr).

At full speed (500,000 rpm or 8,333 Hz) the plant dynamics are dominated by gyroscopic effects. The Bode plots of the plant transfer functions are shown in Figure 5 for this full speed case. Because of the x-y symmetry, the two diagonal or parallel transfer functions (x voltage to x orientation and y voltage to y orientation) are the same. Similarly, the two off-diagonal or cross-coupling transfer functions (x voltage to y orientation and y voltage to x orientation) are also the same. The plant is completely characterized by two transfer functions the parallel (diagonal) and cross (off-diagonal) transfer functions.

These two transfer functions are shown in Figure 5. Two sets of undamped eigenvalues can be seen, one at approximately 16 kHz and the other at approximately 6 Hz. These are both forward whirl modes. The higher frequency whirl mode, or "fast precession mode", is located at the frequency given by the ratio of axial to radial moments of inertia times the rotational speed. At full speed, this open-loop fast precession frequency is 15.8 kHz. The lower frequency whirl

mode, or "slow precession mode", is located at the frequency given by the unstable frequency squared divided by the fast precession frequency. At full speed, this open-loop slow precession frequency is 5.7 Hz. These fast and slow precession modes correspond to similar modes of a "classic" top spinning in a vertical position.

As the rotational speed is increased, these unstable pole pairs gradually take on a whirling nature, as indicated by the growth of the imaginary part of the eigenvalues. At a rotational speed of 320 Hz, the poles reach a stability boundary where formerly unstable modes become purely whirl modes lying on the imaginary axis. As the speed is further increased, the whirl modes split into the "fast precession" and "slow precession" modes as discussed earlier.

5.2 Controller Design

The design approach to develop a fixed-gain controller for this speed varying plant was to first examine how optimal, full-state feedback controllers change with changing plant speed. These full-state feedback controllers assume knowledge of the position and velocity of the rotor in both radial directions. Based on the behavior of these parameter-varying, full-state feedback controllers and the addition of some physical insight, a fixed-gain, full-state feedback controller can be chosen that provides reasonable performance over the full speed range. This full-state feedback controller is then implemented as an output feedback controller using lead-lag compensators to provide estimates of the velocity states. This section outlines this procedure and presents the baseline control algorithm. The following section then presents system simulations.

The first step in this design approach was to develop full-state feedback controllers for various operational speeds. These full-state feedback controllers were designed using the linear-quadratic-regulator (LQR) approach. This controller is the "optimal" initial condition regulator, which closely matches the regulator type performance goals of the controller for the micro-gyroscope.

For the zero-speed LQR design, the desired 1000 Hz bandwidth was achieved with cost-on-control-weighting of $\mu = 0.02$. This resulted in "optimally" damped ($\zeta = 0.707$) closed-loop poles at 1 kHz. Note that at zero speed, the plant is decoupled into separate x and y direction dynamics, as discussed previously. Because of this decoupling, the LQR feedback gains are also uncoupled, and only the "parallel" gains are used. This means that the x-direction torque, for example is a function of only measured x-direction orientation, and x-direction angular velocity. Because of the system symmetry, the same gains are used in the x and y-directions.

The root-locus of the closed-loop eigenvalues, $p_i(\Omega)$, as a function of the rotational speed Ω using this zero-speed state-feedback compensator, K(0), is shown in Figure 6. Shown is a polar plot of the logarithm of the closed-loop frequencies, $\log 10 |p_i|$, and the angle of the poles. Taking the logarithm of the closed loop frequencies makes this plot significantly different than conventional root-loci. The use of the logarithmic magnitude scaling allows the widely divergent closed-loop frequencies of the fast and slow precession poles to both be seen. Because of the logarithm magnitude scaling, vertical lines are not contours of constant real part of p_i, and horizontal lines are not contours of constant imaginary part of p_i, as would be the case in conventional root-loci. Radial lines, however, remain lines of constant damping as for conventional root-loci. Circles about the origin are contours of constant frequency, as is usual, however they are logarithmically scaled.

At zero-speed, as can be seen in Figure 6, the four closed-loop poles for the zero-speed

state-feedback compensator K(0) are paired into two sets of well damped pole pairs with frequency of 6,000 rad/sec (1 kHz). As the rotational speed increases, the poles spilt into two pairs. One pair increases in frequency, the fast precession mode, and one pair decreases in frequency, the slow precession mode. These modes become decreasingly well damped as the speed increases. At full speed they both have damping of approximately 0.1. For this controller, the minimum negative real part of the closed-loop poles occurs at maximum speed in the slow precession mode. For this mode at full speed, the minimum real part of the closed-loop poles is 41 rad/sec.

For the full-speed LQR design, the desired bandwidth of 1000 Hz was achieved with cost-on-control-weighting of $\rho = 0.001$. This is significantly lower than the zero speed case ($\rho = 0.02$) and is a result of the lower plant gain at full-speed, caused by the gyroscopic effects, as discussed earlier. Because of the lower plant gain at full speed, more control effort is needed to achieve a fixed bandwidth, and therefore, less cost must be placed on control effort in the LQR design procedure. At full speed ($\Omega = 8.3$ kHz), the closed-loop poles pairs both have the same real part of -3300 rad/sec. This implies that both modes have the same decay time, a characteristic of this type of LQR approach. One of the pole pairs occurs at the desired bandwidth of 1000 Hz. The other pair occurs at the full-speed fast-precession-frequency of approximately 1×10^5 rad/sec (15 kHz). Because of their different frequencies, these closed loop poles have dramatically different damping ratios as shown in Figure 7.

This full-speed designed controller becomes unstable at low speeds because of the use of cross-proportional feedback. The cross-proportional feedback has the same phase (acts as) damping, however, its effects are not proportional to frequency (velocity) as is conventional damping. Because of this, it acts to dampen (stabilize) forward whirl modes but destabilize backward whirl modes. At full-speed, this is ideal, since the dynamics are dominated by the fast-precession, forward-whirl mode. Because of its use, the minimum real part of the closed-loop eigenvalues at full-speed, is -6000 rad\sec for the full-speed designed compensator as compared to only -41 for the zero-speed designed compensator. At low speeds, however, the use of this level of cross-proportional feedback destabilizes the closed-loop system. At zero speed, for example, the open-loop poles, which describe an inverted, decoupled, two-degree-of-freedom pendulum, can be alternatively described as forward and backward whirl modes. The use of cross-proportional feedback adds stability to the forward whirl mode, but destabilizes the backward mode. Because of this, there is a limit to the amount of cross-proportional feedback that can be used if the system is to operate at zero-speed.

Both the zero-speed, and full-speed state feedback compensators suffer from performance problems when used over the full speed range, as discussed above. The zero-speed state-feedback compensator exhibits slow decay time and low-bandwidth at full-speed. The full-speed state-feedback compensator becomes unstable at low speeds. By using a combination of these compensators, however, a tradeoff can be effected between high-speed performance and low-speed stability. This procedure involved iteratively trying linear combinations of the zero-speed compensator. The design parameters are the ratio of zero-speed to full-speed feedback gains, , and the compensator bandwidths controlled by the cost-on-control-weighting parameters. These parameters were iterated to yield a state-feedback compensator with a minimum of 1000 Hz bandwidth and the largest minimum decay time over the whole speed range. In addition, the ratio between zero-speed and full-speed bandwidth was keep under a factor of 10.

The resulting "best" compensator uses less parallel-proportional gain that the zero-speed design and less cross-proportional gain than the full-speed design. The resulting closed-loop root-locus versus rotational speed is shown in Figure 8 along with the zero-speed case. The "best" compensator has improved damping, as can be seen in Figure 8, and decay time compared to the

zero-speed case.

5.3 Output Feedback Compensator Design and Performance

The full-state-feedback compensator discussed above was then implemented using an output feedback compensator. The full-state-feedback compensator assumes access to the radial angular velocities of the rotor, which are not directly measured. A simple lead-lag compensator is used to combine the parallel proportional and velocity state feedback terms into a equivalent output (measured rotor radial angle) compensator. In addition, critically damped high frequency pole pairs, at a frequency of 600,000 rad/sec (100 kHz) were added to all the compensator transfer functions to roll the system off. As discussed previously, the loop cross-over frequency decreases by almost a factor of ten as the speed increases from zero to full speed. A closed loop frequency response curve for one axis is shown in Figure 9.

5.4 Electronics

5.4.1 Sensor Electronics

The capacitance of the position sensor varies inversely with the distance from the sensor to the target. Over the specified measurement range, the sensor varies in capacitance from approximately 0.027 picofarads (pF) to 0.033 pF. Any stray capacitance on the sensor leads will effect the linearity of the measurement unless the leads are appropriately guarded. The ability to detect position accurately is also hampered by any load placed on the sensor capacitance by the measurement electronics.

The block diagram of the capacitive sensor interface circuit is shown in Figure 10. The sensor is driven by a 100 kHz current source so that the resultant voltage is proportional to the sensor impedance. The AC voltage produced across the sensor is buffered by a "guard" loop, full-wave rectified, and low-pass filtered to produce a DC output voltage directly proportional to distance. The effects of stray capacitance on the sensor leads are greatly reduced by driving the shield of the sensor cable with a "guard" loop. The guard loop drives the shield with a voltage identical to that across the sensor, and thus no current flow is possible. The impedance of the shield is a capacitance greater than 200 pF to ground. In order to drive this load, the voltage across the sensor is buffered by the FET input stage, a high-bandwidth differential op-amp, and a high-current buffer. The bandwidth of this follow-up loop must be high to reduce any effects of the guard capacitance upon the sensor capacitance. To reduce the input capacitance of the sensor electronics, a Field Effect Transistor (FET) input stage is used. This input stage presents a very high resistance and low capacitance load to the sensor. The FET input stage is configured as a source-follower where the source signal will exactly follow the gate (input) signal. The source terminals of the FETs are each loaded with a transistor current source. The high impedance of the current sources reduces the effect of any gate-to-source capacitance. The drain of the FETs are capacitively coupled to the buffered sensor voltage to reduce the effects of any gate-to-drain capacitance. Stray capacitance on the circuit board would be reduced by placing the buffer-loop circuitry on a copper-clad board with the copper clad driven by the guard voltage. The output of the sensor guard-loop is bandpass filtered to eliminate both DC drift and high-frequency noise effects. The signal is then full-wave rectified and low-pass filtered to produce a DC output voltage. The filter is a four-pole Butterworth, and contributes less than 10 degrees of phase error at the loop cross-over frequency.

5.4.2 Control and Read-Out Electronics

Control and read-out of the micro-gyro is accomplished simply with six op-amps: three for tilt control around the x-axis and three for y as shown in Figure 11. The first op-amp finds the difference in the signals from the capacitive sensor electronics which results in a measure of the tilt angles. The parallel-axis angle measurement is fed to the compensation stage through a lead-lag network which provides proper gain and phase margin at the loop-crossover frequency of the tilt loop. The cross-axis angle measurement is also summed into the compensation stage in order to compensate for the gyroscopic coupling between the axes. The feedback network of the compensation stage includes integral gain which ensures virtually-zero error at dc, and a high frequency pole to reduce both noise and sensitivity to unmodelled dynamics. The output of the compensation stage is fed to the two actuator drive stages where it is respectively added to and subtracted from a dc bias voltage. This differential operation about a bias voltage linearizes the electrostatic actuator. This makes the output of the compensation stage proportional to the restraint torque, and thus proportional to the input rate. Due to the electrostatic actuator requirements, the actuator driver stages are high-voltage op-amps capable of 120 volt output.

5.4.3 Motor Drive Electronics

The gyro wheel-motor is a three-phase bipolar variable-capacitance motor. Since this motor type is synchronous, i.e., produces torque only when the rotation frequency and excitation frequency are the same, it requires a variable-frequency drive source. In addition, the push-pull excitation required for each of the three bipolar phases will require six high-voltage output stages.The motor is driven with balanced bipolar voltages so that the rotor will remain near ground potential. Any voltage induced on the rotor will cause it to be strongly attracted to the grounded substrate because of its large surface area.

Motor start-up will require that the excitation frequency start at the sub-Hertz level and ramp up to the full-speed value of 25 kHz. This is accomplished with a ramp generator and voltage-to-frequency (V/F) converter. The bipolar three-phase generator takes the single-phase output of the V/F converter and produces three square-waves with 120 degrees phase difference and their complementary signal for driving the output stages. In addition, the circuit generates the signal pair which develops the bipolar waveforms. The output circuit contains six high-voltage drivers, one for each bipolar phase, and can deliver up to 120V.

6. Fabrication

This Section outlines a sequence for fabrication of the micro-gyro described above. The steps described here follow established surface micro-machining procedures as practiced at MIT. Though all of the processes described here have been performed before, their combination into the micro-gyro will be a significant advancement in the state of the art. The numbered steps and Figure 12 below show the fabrication sequence.

1) The rotary micro-gyro fabrication process begins with <100>, p-type silicon wafers. P-type wafers are chosen to allow the selective ion implantation of phosphorus for control electrodes in step 3.

2) The next steps involve etching the center pin in which the rotor will rest. A 500 Å silicon nitride etch mask must be deposited in order to define the height of the pin (Figure 12). An HF isotropic etch with no agitation will yield a shallow bottomed etch area. The etchant will undercut the edges of the Silicon Nitride mask and form a conical point beneath it. The etch is done when the nitride pattern disappears. Some experimentation will be required to determine the correct pattern diameter to produce the desired pin height after etching.[4]

3) This step is the selective ion implantation of phosphorous on the silicon wafer. This yields n-type regions which form the lower control electrodes. Note that when the electrodes are energized with a positive voltage on the p-type material, a reversed-bias diode is formed between the electrode material and the rest of the substrate yielding electrical isolation.[5]

4) A thin layer (0.5 μ) of LTO (low temperature silicon dioxide) is deposited next to form the first sacrificial spacer layer. On top of this layer is deposited 0.5 μ of poly-crystalline silicon (polysilicon). The polysilicon is heavily doped with phosphorus and patterned to form the rotor's control electrode.

5) The next material that is deposited is silicon nitride which will yield electrical isolation between the substrate and the stator drive electrodes and also between the rotor's control and drive electrodes. Before this can be done, windows in the first sacrificial layer (LTO #1) must be opened so that the silicon nitride layer will bond to the substrate. A 1000 Å thick layer of LPCVD stoichiometric silicon nitride can now be deposited and patterned. Note that if a thicker layer of nitride is determined to be required for improved electrical insulation, the large tensile residual stress of the stoichiometric material could cause warping of the released structure. To reduce the stress in such a case, the nitride should be deposited in a silicon rich form[6].

6) The main rotor and stator structure is now deposited in the form of a 2.5 μ layer of LPCVD polysilicon. Once again the polysilicon is heavily doped with phosphorus to make it a good conductor. The patterning of this layer defines not only the rotor and stator pole configuration, but also the rotor--stator gap spacing. The current state of the art allows for aspect ratios of rotor thickness to rotor-stator gap spacing of about 2 to 1. Considerable process development would be required if this aspect ratio must be increased significantly.

7) The last steps in the process are used to fabricate tabs which keep the rotor in place after the final release. A second layer of sacrificial oxide (LTO #2) is deposited to a thickness of approximately 1 μ. The layer is patterned (mask #7) to open holes through which the polysilicon hold--down tabs will bond to the stator poles (poly #2). Next, 1 μ of LPCVD polysilicon is deposited an patterned to form the hold--down tabs (mask #8).

8) The final step in the fabrication process is the removal of the sacrificial oxide to release the rotor. This is accomplished with a simple HF timed etch. In order to keep the etch time from becoming excessive, the rotor may need to have holes strategically placed to reduce the distance that the etchant must undercut.

6. Conclusions

The results of this program are very positive. Though extensions of fabrication technology will be required for fabrication of a fully suspended microgyroscope, the potential for successful development is very good. The fabrication of a simplified top arrangement can be achieved with current technology and was studied in depth as an initial control and electronics testbed. An operational micromechanical gyroscope would have many applications in commercial, aerospace, and military sectors.

REFERENCES

1. Howe et all, "Silicon micromechanics: sensors and actuators on a chip", IEEE Spectrum, July

1990.

2. S. Bart, Modeling and Design of Electroquasistatic Microactuators, PhD Thesis, Massachusetts Institute of Technology, Cambridge MA , September 1990.

3. M. Schmidt, et all, "Surface micromachining of polyimide/metal composites for a shear-stress sensor", in IEEE Micro Robots and Teleoperators Workshop, Hyannis MA, 1987.

4. K. Petersen. "Silicon As A Mechanical Material". Proc. IEEE, 70(5):420-457, May 1982.

5. L. Tavrow, "A LOCOS-Based Microfabricated Radial-Gap Electric Motor" PhD Thesis, Massachusetts Institute of Technology, Cambridge MA, 1991.

6. H. Guckel, D.K. Showers et all, "Deposition Techniques and Properties of Strain Compensated LPCVD Silicon Nitride Films", In Technical Digest of the IEEE Solid-State Sensor and Actuator Workshop, Hilton Head Island SC, 1986.

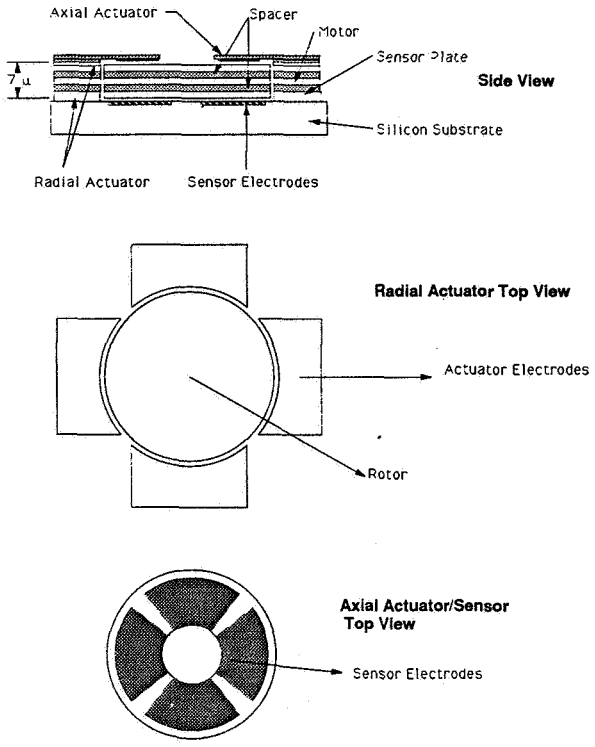

Figure 1. Fully suspended configuration

μ Gyro Block Diagram
3/15/91

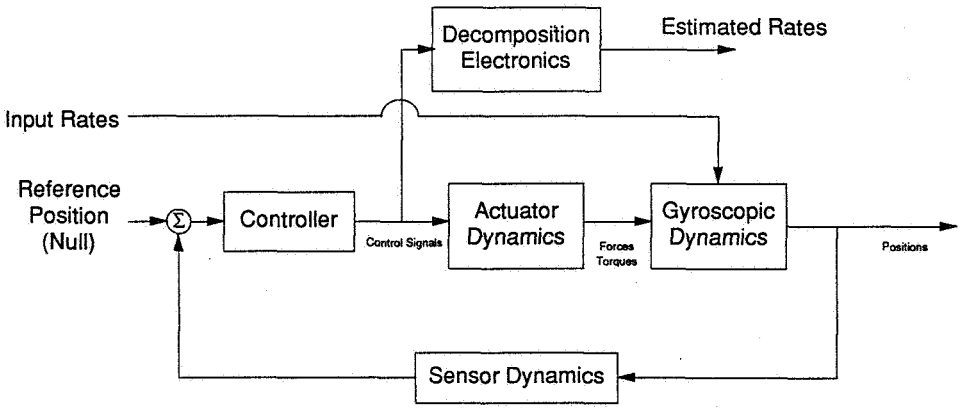

Figure 2. System block diagram

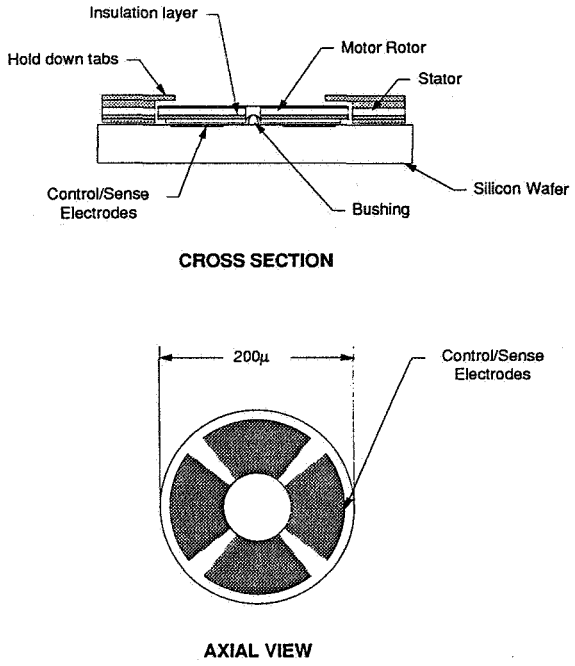

Figure 3. Top configuration

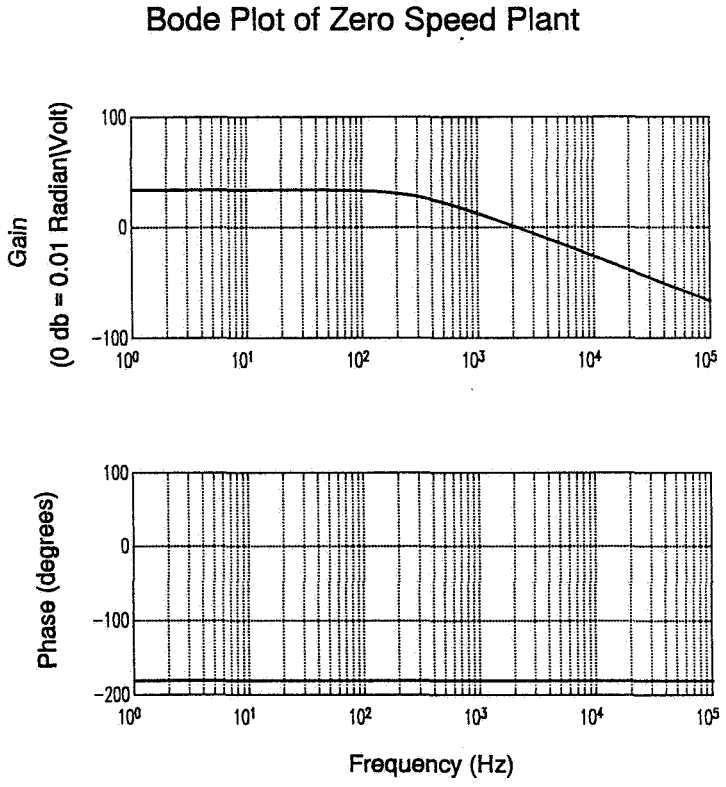

Figure 4

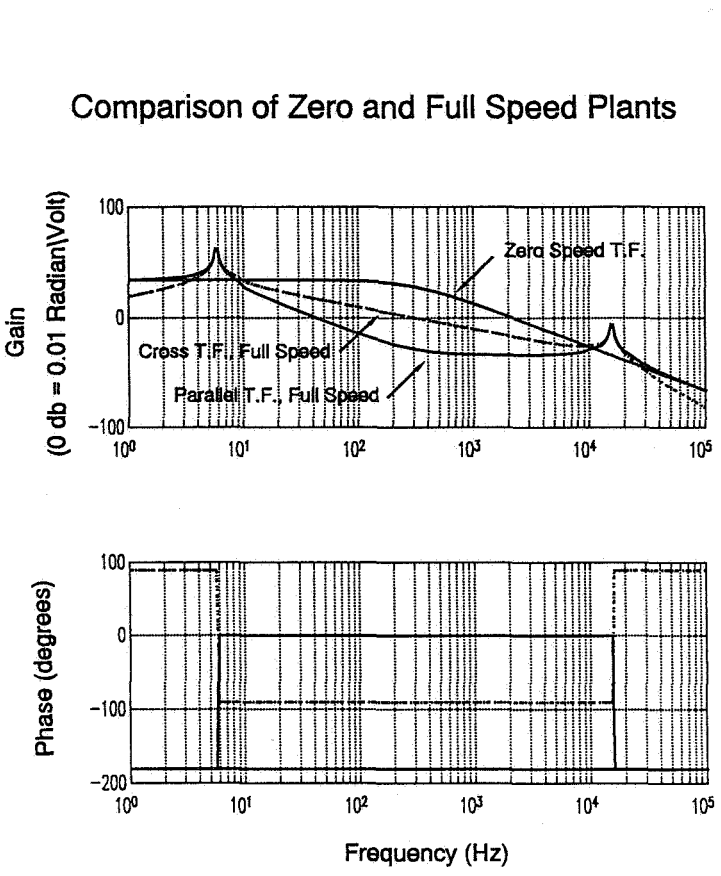

Figure 5

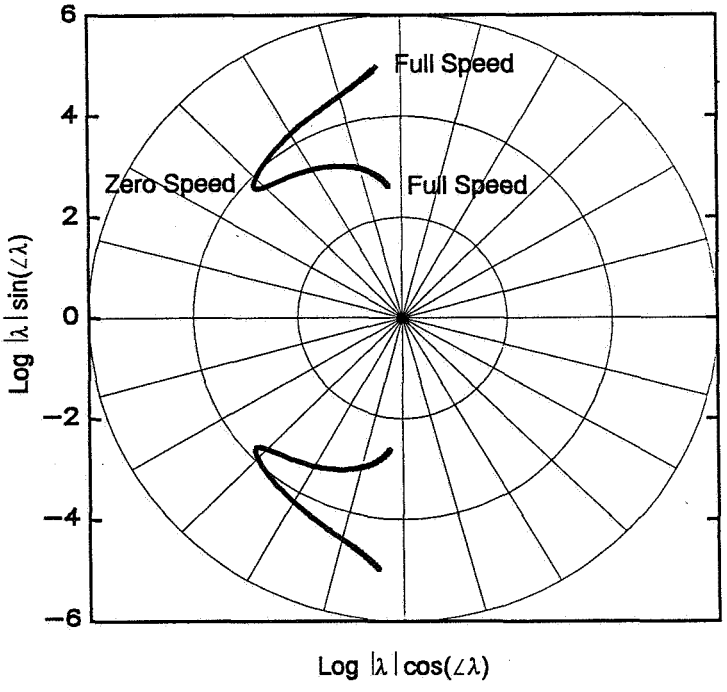

Figure 6

Root Locus of "Full Speed" Controller

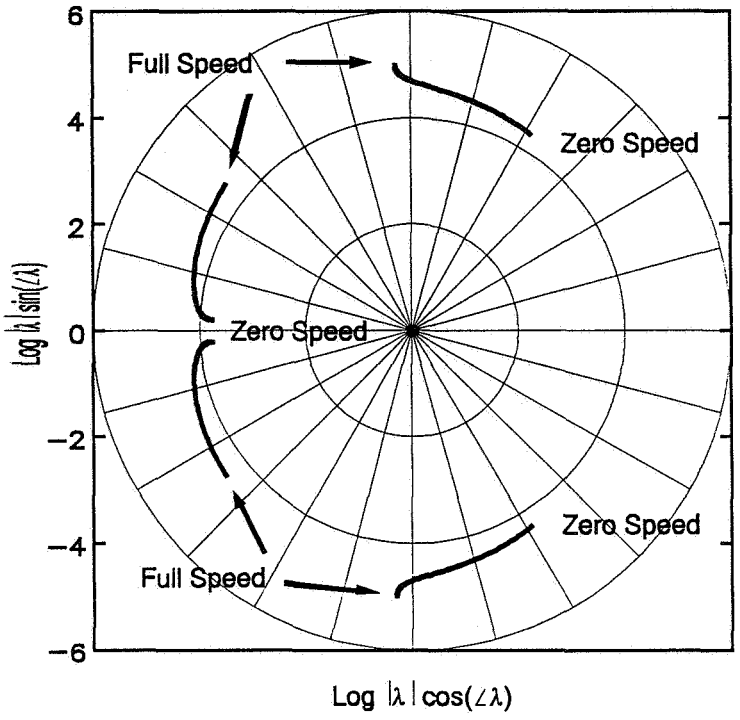

Figure 7

Comparison of "Best" and "Zero Speed" Controller

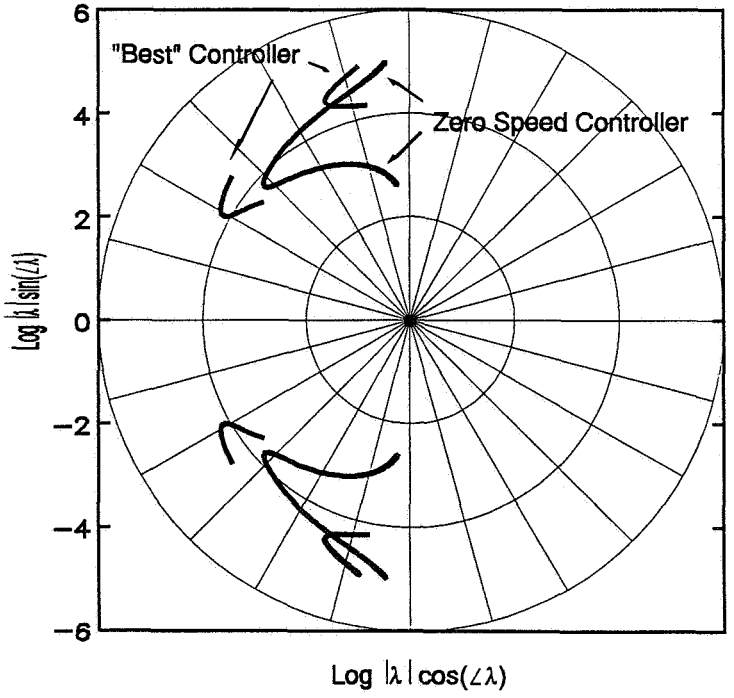

Figure 8

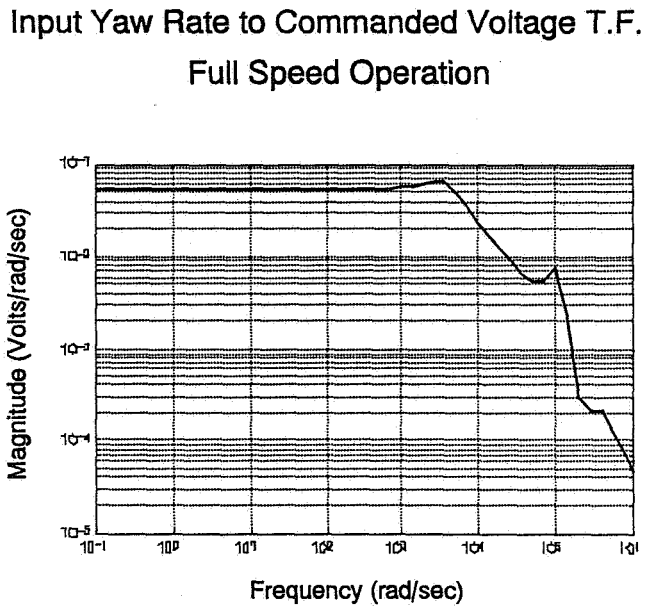

Figure 9

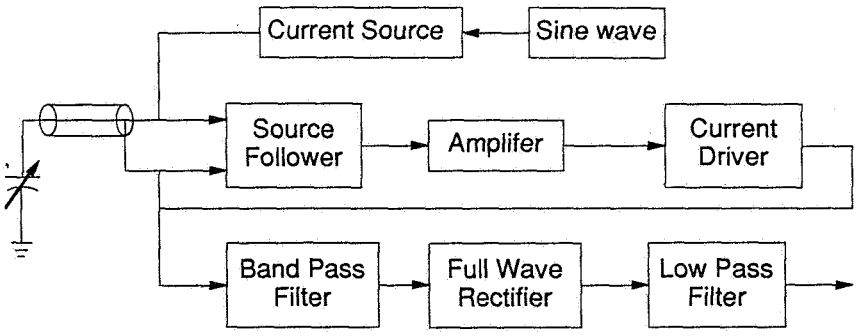

Figure 10. Capacitive sensor block diagram

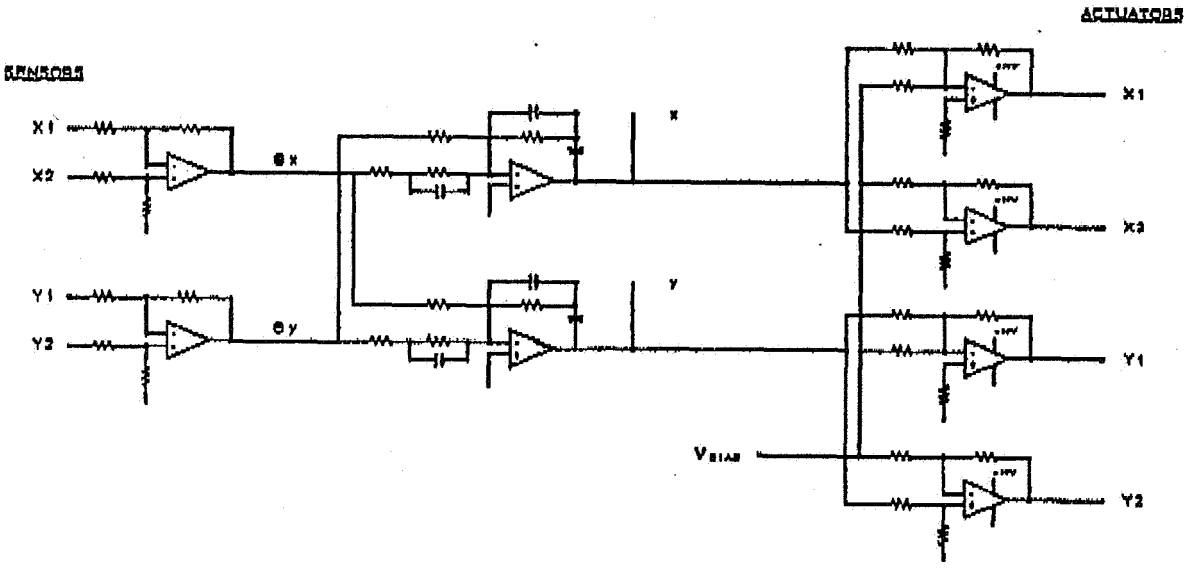

Figure 11. Readout electronics diagram

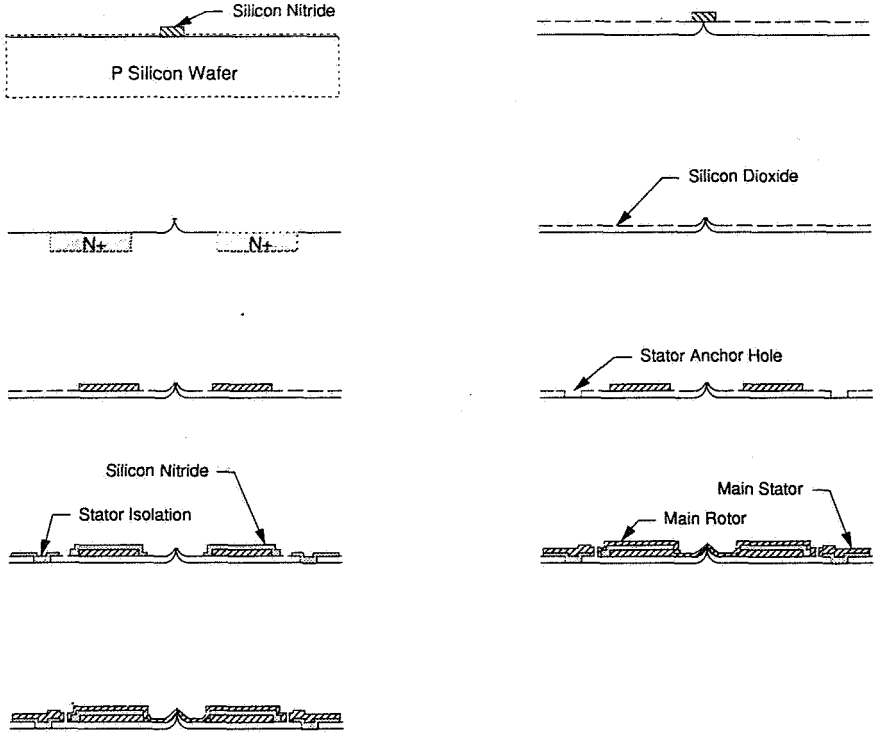

Figure 12. Fabrication sequence